Systems biology-enabled targeting of NF-κB and BCL2 overcomes microenvironment-mediated BH3-mimetic resistance in DLBCL.

Running title: Disentangling NF-κB and BCL2 in DLBCL

Aimilia Vareli[1], Haripriya Vaidehi Narayanan[2], Heather Clark[1], Eleanor Jayawant[1], Hui Zhou[3], Yi Liu[3], Lauren Stott[1], Fabio Simoes[1], Alexander Hoffmann[2], Andrea Pepper[1], Chris Pepper[1], Simon Mitchell[1†].

[1] Department of Clinical and Experimental Medicine, Brighton and Sussex Medical School, Falmer, United Kingdom; [1] Department of Clinical and Experimental Medicine, Brighton and Sussex Medical School, Falmer, United Kingdom; [2]Signaling Systems Laboratory, Department of Microbiology, Immunology, and Molecular Genetics, and Institute for Quantitative and Computational Biosciences, University of California, Los Angeles, Los Angeles, CA, United States; [3]DeepKinase Biotechnologies, Beijing, China

[†] S.A.Mitchell@bsms.ac.uk

Abstract: 198 words

Text: 4000 words

Figures: 7

References: 57

21 **Key Points**

22 - TME-mimicking co-culture provides resistance to BH3-mimetics through BCLXL, which can
23 be overcome by inhibition of non-canonical NF-κB.
24 - Multidisciplinary profiling reveals how high NF-κB activity leads to crosstalk, and BH3-
25 mimetic resistance counteracted by BTK inhibition.

26 **Abstract**

27 In Diffuse Large B-cell Lymphoma (DLBCL), elevated anti-apoptotic BCL2-family proteins (e.g.,
28 MCL1, BCL2, BCLXL) and NF-κB subunits (RelA, RelB, cRel) confer poor prognosis. Heterogeneous
29 expression, regulatory complexity, and redundancy offsetting the inhibition of individual proteins,
30 complicate the assignment of targeted therapy. We combined flow cytometry 'fingerprinting',
31 immunofluorescence imaging, and computational modeling to identify therapeutic vulnerabilities in
32 DLBCL. The combined workflow predicted selective responses to BCL2 inhibition (venetoclax) and
33 non-canonical NF-κB inhibition (Amgen16). Within the U2932 cell line we identified distinct
34 resistance mechanisms to BCL2 inhibition in cellular sub-populations recapitulating intratumoral
35 heterogeneity. Co-cultures with CD40L-expressing stromal cells, mimicking the tumor
36 microenvironment (TME), induced resistance to BCL2 and BCLXL targeting BH3-mimetics via cell-
37 type specific upregulation of BCLXL or MCL1. Computational models, validated experimentally,
38 showed that basal NF-κB activation determined whether CD40 activation drove BH3-mimetic
39 resistance through upregulation of RelB and BCLXL, or cRel and MCL1. High basal NF-κB activity
40 could be overcome by inhibiting BTK to resensitize cells to BH3-mimetics in CD40L co-culture.
41 Importantly, non-canonical NF-κB inhibition overcame heterogeneous compensatory BCL2
42 upregulation, restoring sensitivity to both BCL2- and BCLXL-targeting BH3-mimetics. Combined
43 molecular fingerprinting and computational modelling provides a strategy for the precision use of
44 BH3-mimetics and NF-κB inhibitors in DLBCL.

45 **Introduction**

46 Diffuse large B-cell lymphoma (DLBCL), is an aggressive blood cancer (1). First line treatment is only
47 successful in approximately 60% of patients (2, 3). Escalated treatment regimens have not improved
48 overall survival (4, 5). The highly heterogenous nature of the disease has challenged advancing the
49 standard of care through one-size-fits-all approaches (6-11). Activated B-cell (ABC) DLBCL patients
50 bearing Nuclear Factor-κappa light chain enhancer of B cells (NF-κB) activating mutations, and
51 Germinal Center (GC) DLBCL patients with *BCL2*-activating mutations have particularly poor
52 prognosis (11). As such, both NF-κB and B-cell leukemia/lymphoma 2 protein (BCL2)-family proteins
53 are central to poor prognosis DLBCL.

54 NF-κB is a dimeric transcription factor composed of combinations of five proteins (RelA, RelB, cRel,
55 p50 and p52), which are normally sequestered in the cytoplasm by a combination of four inhibitors
56 of NF-κB (IκBα, -β, -δ, and-ε) (12, 13). The IκB proteins have distinct affinities for different NF-κB
57 dimers with IκBα predominantly inhibiting RelA-containing dimers and IκB-δ and -ε regulating cRel-
58 containing dimers in a context-specific manner (14, 15). The abundance and nuclear localization of
59 individual NF-κB components have been found to be prognostically informative in DLBCL (16-18).
60 Heterogeneity in NF-κB subunits can be quantified and visualized using flow cytometry to reveal
61 unique 'fingerprints' of NF-κB, with heterogenous levels of individual NF-κB proteins found within
62 ABC-DLBCL (19). Two NF-κB pathways (canonical and non-canonical) may be activated by a
63 combination of tumor microenvironmental signaling and activating mutations in DLBCL leading to
64 nuclear translocation of NF-κB (20). While targeting NF-κB has shown therapeutic potential in
65 subgroups of blood cancer patients (21-26), heterogeneity and toxicities associated with global
66 targeting of the canonical NF-κB pathway, has challenged clinical progress. The oncogenic role of
67 NF-κB in lymphoma is largely attributed to the anti-apoptotic gene expression induced upon NF-κB
68 activation (26, 27).

69 Anti-apoptotic BCL2 family proteins, including Myeloid Cell Leukemia 1 (MCL1) and B-cell
70 Lymphoma-extra Large (BCLXL), are inhibitors of the intrinsic pathway of apoptosis (28, 29), and are
71 often overexpressed in DLBCL as a result of gene translocation events, gene amplifications,
72 mutations within open reading frames, and microenvironment-mediated increased NF-κB activity
73 (30). BCL2 is an attractive target in DLBCL, and the specific BCL2 inhibitor venetoclax is clinically
74 used alongside chemotherapy for the treatment of CLL, acute myeloid leukemia (AML) and other
75 hematological malignancies (31). However, venetoclax has shown limited efficacy in clinical trials
76 (31, 32). BCL2-family proteins (MCL1 and BCLXL) are often over expressed in DLBCL with elevated
77 expression conferring venetoclax resistance by compensating for the sequestration of BCL2 (33, 34).
78 The daunting complexity of both NF-κB regulatory networks, and apoptotic signaling regulation, has
79 motivated the use of computational systems biology models to predict responses to BH3-mimetics
80 (35), responses to the TME (19, 36), and predict the impact of mutations on clinical outcome (19, 37).
81 A predictive understanding of how heterogeneity in NF-κB activity results in anti-apoptotic protein
82 heterogeneity in the context of the tumor microenvironment (TME), and controls response to BH3-
83 mimetics has the potential unlock the deployment of targeted therapies such as BH3-mimetics and
84 NF-κB inhibitors. Here, we aimed to assess if NF-κB and BCL2 family 'fingerprinting' could be a
85 predictor of sensitivity to BH3 mimetics and/or NF-κB inhibition in DLBCL. We aimed to investigate
86 the effect of the TME-mediated NF-κB activation on sensitivity to BH3-mimetics inhibition and
87 establish computationally enabled therapeutic strategies to overcome TME-mediated therapy
88 resistance through targeting NF-κB.

89 **Methods**

90 **Mice**

91 Primary B cells were acquired from C57BL/6, C57BL/6 IκBε$^{-/-}$ and C57BL/6 IκBα^{mut} female mice (9-12
92 weeks old), spleens were homogenized and splenocytes were stained with anti-CD43, prior to

93 purification by negative column selection (Miltenyi Biotec, Cologne Germany) as described (14, 38).
94 B cell purity was assessed by flow cytometry staining for anti-B220. Mice were maintained in
95 environmental control facilities at the University of California, Los Angeles. Animal work was
96 performed according to University of California, Los Angeles regulations, under an approved
97 protocol.

98 **Cell culture**

99 DLBCL cell lines were sourced from DSMZ (Braunschweig, Germany) and cultured in recommended
100 medium. Cells were kept at 37°C in 5% CO_2 conditions and routinely tested for mycoplasma
101 contamination. NIH3T3 cells transfected to stably express human CD40 (hCD40L-3T3) were
102 obtained from Prof Chris Pepper (Brighton and Sussex Medical School, UK) and transfection was
103 maintained by puromycin selection (0.1%).

104 **Co-culture**

105 DLBCL cells were co-cultured with hCD40L-3T3, or non-transfected control cells for 24 hours on 96-
106 well flat bottom plates, with or without small molecule inhibitors.

107 **Drug Treatments**

108 0.1 x 10^5 DLBCL cells were plated per well and treated with Amgen16 used at concentrations of 1.25-
109 100μM purchased from Merck (Gillingham, UK) . ABT199 (venetoclax) was purchased from
110 Selleckchem (Texas, USA) and used at concentrations of 0.0001-100μM with or without Amgen16 at
111 a dose of 50μM for 24 hours.

112 **Flow Cytometry**

113 Early apoptosis was determined by flow cytometry following Annexin V staining (BioLegend) and data
114 was acquired on a CytoFlex LX, using the BD fix and perm kit (BioLegend), and data was acquired as
115 previously described (19).

116 **Proteomics**

117 Equal amounts of protein determined using BCA assay, from each sample were digested using
118 trypsin. For tyrosine phosphoproteomics, peptides were enriched using SH2-superbinder beads as
119 described (39), and the flow-through reconstituted in freshly prepared sample loading buffer and
120 subjected to phosphopeptide enrichment using TiO_2 beads preconditioned with the loading buffer
121 for 5 minutes. Data-independent acquisition mass spectrometry (DIA-MS) experiments were
122 performed on a ThermoFisher Orbitrap Astral mass spectrometer. A DIA spectral library generated
123 using DIA-MS2pep was utilized in DIA-NN software for protein quantification, with precursor and
124 protein false discovery rates (FDR) set to 1%. Heatmaps were generated using R package pheatmap
125 (version 1.0.12).

126 **Immunofluorescent Microscopy**

127 NF-κB activity was determined post fixation with 4% PFA and permeabilization with 0.1% Triton-X.
128 Cells were stained with anti-p65 (Invitrogen), RelB (Cell signaling), cRel (Invitrogen), DAPI
129 (ThermoFisher) and rhodamine phalloidin (Thermo Scientific). Images were captured with *Operetta*
130 *CLS*, and nuclear:cytoplasmic ratios of NF-κB proteins were analyzed with *Cell Profiler*.

131 **Computational**

132 The computational model and simulation method is described previously (36). Basal canonical
133 pathway activation was increasing 0% to 0.5%. NIK degradation was decreased using the equation
134 *NIK deg=1/(1+(t/600))*. 25 individual simulations were run for each cell line with parameter sampling
135 as described previously (36, 40). Models were solved using the Julia DifferentialEquations.jl package
136 (41).

137 **Statistical Analysis**

138 All statistical analysis was performed using GraphPad Prism 10.0 (California, USA) and Julia 1.8.5.
139 Analysis of paired datasets was performed with paired t-tests, whereas unpaired t-tests and one-way
140 ANOVA to analyze differences between groups, followed by indicated post-hoc tests. LC_{50} values

141 were generated a post four-parameter linear regression test. Flow cytometry data was analyzed on
142 CytExpert Software (Beckman Coulter). *P<0.5; **P<0.01; ***P<0.001; ****P<0.0001.
143
144 **Results**
145 **Flow cytometry-based 'fingerprinting' predicts sensitivity to inhibitors targeting non-canonical**
146 **NF-κB and BCL2**
147 Previous work in which NF-κB subunit abundance was visualized as contoured density plots standardized
148 using z-scores (Figure 1A) established heterogeneity in RelA abundance between ABC-DLCBL cell lines
149 (19). To establish whether similar variability is present in ABC- and GC-DLBCL we measured the levels of
150 NF-κB in two ABC- (RIVA and U2932) and two GC-DLBCL (SUDHL8 and SUDHL10) cell lines (Figure 1B),
151 and identified varied expression of both RelA and RelB, which did not align with COO (Figure 1B). While
152 there was no variability in RelB between ABC cell lines (RIVA and SUDHL8, Figure 1C), as reported
153 previously (19), GC-DLBCL cell line SUDHL10 was found to have significantly higher RelB (Figure 1B and
154 C) and a higher ratio of RelB to RelA (Figure 1B). We hypothesized that this cell line may be sensitive to NIK
155 inhibition, and found NIK-inhibitor Amgen16 was significantly more effective at killing SUDHL10 cells than
156 cell lines with lower levels of RelB (Figure 1D and E, p<0.01).
157 We next sought to establish whether a similar approach could enable predictable targeting of BCL2-family
158 proteins. We identified two lines with low BCL2 (SUDHL8, and SUDHL10, Figure 1F), and two lines with
159 significantly higher BCL2 (U2932, and RIVA, Figure 1G, p<0.0001). In agreement with clinical observations
160 (31), we found that ABT199 had significantly higher efficacy in cell lines with high BCL2 (Figure 1H and I,
161 p<0.01). While SUDHL10 cells resist ABT199 due low BCL2, the NF-κB profiling (Figure 1B) revealed a
162 vulnerability to NIK inhibition (Figure 1D-E), indicating the potential for combined NF-κB and BCL2
163 "fingerprinting" to inform the rational assignment of therapeutic agents targeting multiple pathways in
164 DLBCL.
165

166 **BCL2 family protein heterogeneity confers heterogenous responses to ABT199 within a biclonal**
167 **DLBCL cell line**

168 The U2932 cell line harbors two phenotypically and genetically distinct subclones. The subclone R1
169 is CD20, CD38 high and characterized by BCL6 upregulation, while the R2 subclone is CD20, CD38
170 low and characterized by MYC upregulation (19, 42). We found that the R1 subclone was ABT199
171 resistant, whereas the R2 subclone was ABT199 sensitive, even at the lowest dose of ABT199 tested
172 (0.0001μM) (Figure 2B). BCL2 protein abundances did not differ between the two subclones and
173 therefore could not explain the different sensitivities to ABT199 (Figure 2C). However, we identified
174 significantly higher MCL1 in the R1 subclone (Figure 2C, $p<0.0001$). We wondered if the selective
175 sensitivity of the R2 subclone to ABT199 would be retained when DLBCL cells are activated by their
176 TME (33, 34). For this purpose, we employed a co-culture system of hCD40L-3T3, which has been
177 established to mimic the lymph node TME in multiple studies through recreating both cell-contact
178 and the presence of activated T cells in the DLBCL TME (24, 43)(Figure 2D). The R2 subclone became
179 substantially more resistant in the co-culture system (Figure 2E). We found a significant increase in
180 resistance to ABT199 in the hCD40L-3T3 co-culture (Figure 2F, $p<0.01$). We measured the anti-
181 apoptotic proteins induced by hCD40L-3T3s and found the fold change in BCLXL was significantly
182 higher than both BCL2 ($p<0.05$) and MCL1 ($p<0.01$) which were either unchanged (BCL2) or
183 moderately decreased (MCL1) compared to monoculture (Figure 2G). Within the U2932 cell lines we
184 identified multiple distinct resistance mechanisms to ABT199; high MCL1 in the R1 subclone, and
185 high BCLXL in the context of CD40L co-culture.

186 **TME-mediated resistance to BH3-mimetics can result from induction of multiple compensatory**
187 **BCL2-family proteins**

188 To determine whether TME-mediated venetoclax resistance and BCLXL upregulation was a feature
189 unique to U2932 cells, we repeated this analysis in the BCL2-dependent RIVA cells (Figure 3A). We

190 found significant TME-mediated ABT199 resistance in hCD40L-3T3 co-culture with over 3 orders of
191 magnitude higher LC_{50} than monoculture (Figure 3B, $p<0.05$) and a significant increase in BCLXL
192 (Figure 3C, $p<0.01$). This effect was dependent on CD40L as co-culture with untransfected NIH3T3s
193 did not upregulate BCLXL in either cell line (supplemental Figure 1,2 and 4).
194 To establish whether TME-mediated resistance to BH3-mimetics through compensatory
195 upregulation of BCL2-family proteins was unique to venetoclax we employed the SUDHL8 cell line,
196 which has established sensitivity to BCLXL inhibition with the BH3- mimetic A1331852 (34). SUDHL8
197 cells were rendered significantly resistant to BCLXL inhibition in hCD40L-3T3 co-culture (Figure 3D-
198 E, $p<0.001$). Significantly more MCL1 was induced than either BCLXL or BCL2 in hCD40L-3T3 co-
199 culture (Figure 3F, $p<0.05$). This effect was not seen in co-culture with untransfected NIH3T3s
200 (supplemental Figure 3 and 4). While CD40 is known to activate non-canonical NF-κB signaling
201 component RelB, which has been shown to control BCLXL expression in related hematological
202 malignancies (25), the control of MCL1 by specific NF-κB subunits is less clear, particular in the
203 context of lymphoma.
204 **The SUDHL8 cell line has high basal nuclear NF-κB RelA activity through elevated B cell receptor**
205 **signaling.**
206 We hypothesized that the canonical RelA- or cRel-containing NF-κB dimers could be responsible for
207 cell line-specific induction of BH3-mimetic resistance through MCL1 (Figure 4A). Therefore, we
208 sought to quantify the nuclear activity of NF-κB RelA and cRel using immunofluorescence
209 microscopy in cell lines that preferentially induce BCLXL (RIVA and U2932) and cell lines that
210 preferentially induce MCL1 (SUDHL8, Figure 4B, analysis pipeline supplemental Figure 5). This
211 imaging revealed substantial cell-to-cell variability in nuclear NF-κB activity (Figure 4C) and double
212 the average nuclear RelA in the SUDHL8 cell line (Figure 4D, bottom).

213 We performed global, and serine threonine proteomics in the cell line with elevated nuclear RelA
214 (SUDHL8), a line with low nuclear RelA (U2932), and a line dependent on non-canonical signaling
215 (SUDHL10), to test whether elevated B Cell Receptor (BCR) signaling was responsible for elevated
216 nuclear RelA. These data show substantially elevated CD19 and SYK abundance and
217 phosphorylation levels in SUDHL8 compared to U2932 and SUDHL10 (supplemental Figure 6A-B).
218 BTK abundance in SUDHL8 was not elevated; however, phosphorylated Y223 in the BTK SH3 domain
219 has recently been found to mirror catalytic activity (44). Therefore, we also performed
220 phosphotyrosine (pY) proteomics, which revealed elevated phosphorylation at BTK_Y223 in SUDHL8
221 cells (1.8 fold) consistent with elevated BTK activity (supplemental Figure 6C).
222 As CD40L is a selective activator of non-canonical NF-κB signaling in B cells (45), it is not clear how
223 elevated BTK activity and RelA nuclear abundance in SUDHL8 could confer CD40-mediated
224 induction of MCL1 (Figure 4A). IκBα, IκBε, and p100/IκBδ are all induced by RelA activity (12), and are
225 preferential inhibitors of distinct NF-κB subunits (Figure 4A)(14, 36, 38). Therefore, we hypothesized
226 that the altered profile of NF-κB inhibitors present when NF-κB RelA is constitutively active could
227 confer distinct responses to the TME, and sought to establish how this could lead to selective
228 induction of MCL1.

229 **Computational modelling informed by imaging experiments predicts that high basal nuclear**
230 **NF-κB RelA leads to crosstalk, with CD40-mediatead induction of cRel**

231 We employed established computational models of NF-κB signaling (19, 36), and ran two
232 simulations differing only in the degree to which basal BCR-signaling was elevated to recapitulate
233 the constitutive nuclear RelA activity seen in SUDHL8 cells, and low nuclear RelA seen in RIVA cells.
234 Plotting the predicted composition of NF-κB inhibitors bound to both RelA:p50 (Figure 5A, left)
235 revealed that RelA:p50 is mainly inhibited by IκBα in RIVA cells (Figure 5A), with SUDHL8 cells having
236 reduced total inhibition of RelA and a moderate shift in inhibitor composition (away from IκBα and

237 IκBε, Figure 5A–left). The predicted impact of high basal canonical pathway activation on cRel:p50
238 was markedly different (Figure 5A, right), shifting towards IκBδ inhibition of cRel in SUDHL8 cells,
239 with <10% of cRel being inhibited by IκBα and -ε (Figure 5A right).
240 Simulations of the virtual SUDHL8 and RIVA cell lines (Figure 5B), demonstrated that the steady state
241 of these simulations (Figure 5B, t=0) recapitulated the selectively elevated nuclear RelA, with no
242 difference in cRel, as seen in immunofluorescence imaging (Figure 4D). Simulating the impact of co-
243 culture mediated non-canonical pathway activation revealed induction of RelB:p52, without
244 induction of RelA:p50 (Figure 5B, left and center). However, a striking induction of nuclear cRel:p50
245 was predicted to occur only in the SUDHL8 cell line (Figure 5B, right). Cells with low basal nuclear
246 RelA, such as RIVA cells, reliably induce p100 processing to p52, and subsequent translocation of
247 RelB:p52 to the nucleus upon CD40L activation (Figure 5C). Simulations predict that constitutive
248 activation of the BCR pathway results in degradation of IκBα and IκBε, nuclear translocation of
249 RelA:p50 and subsequent induction of p100, which forms higher molecular weight inhibitory
250 complexes termed IκBδ (13). IκBδ has higher affinity for cRel than RelA (14), resulting in sequestration
251 of cRel by IκBδ prior to CD40L activation (Figure 5D, left). Upon CD40L activation p100 is processed
252 into a self-inhibited p100:p52 dimer, which frees cRel for nuclear translocation (13, 38) (Figure 5D,
253 right). This crosstalk mechanism was first identified in fibroblasts (13), and shown to preferentially
254 upregulate cRel in proliferating healthy B cells responding to BAFF (38). This predicted crosstalk from
255 non-canonical signaling to NF-κB cRel has not previously been described in lymphoma linked to
256 induction of anti-apoptotic proteins, therefore we sought to validate these computational
257 predictions.
258
259 **Experimental validation of modelling predictions confirms crosstalk between CD40 and cRel**
260 **confers BH3-mimetic resistance and can be overcome with BTK inhibition**

261 Immunofluorescence imaging of RelA, RelB and cRel confirmed that hCD40L co-culture did not
262 induce RelA (Figure 5E-F, compare to 5B left), but did induce significantly higher levels of
263 nuclear:cytoplasmic RelB in both the RIVA and SUDHL8 cell lines, as predicted by computational
264 simulations (Figure 5E-F, compared to 5B middle, $p<0.05$). Only in SUDHL8 cells was this
265 accompanied by significantly increased nuclear cRel, as predicted computationally (Figure 6E-F,
266 compared to 5B right, $p<0.01$). These combined computational predictions and experimental
267 validation indicated that SUDHL8 cells have higher basal RelA activity, which renders them
268 susceptible to crosstalk between CD40L-mediated activation of the non-canonical pathway and
269 cRel. To confirm that BCR-pathway activation was responsible for BH3-mimetic resistance in the
270 SUDHL8 cells, we tested the ability of the canonical NF-κB inhibitor Ibrutinib (targeting BTK) to
271 overcome TME-mediated resistance to the BCLXL inhibitor A1331852 (Figure 6G). hCD40L co-culture
272 with the addition of ibrutinib, confirmed canonical pathway inhibition re-sensitized SUDHL8 cells to
273 BCLXL inhibition (Figure 5H, $p<0.001$).
274
275 **NF-κB cRel activity selectively induces MCL1 in B cells**
276 We hypothesized that crosstalk-mediate induction of cRel was responsible for the induction of MCL1
277 (Figure 3F). We investigated ChIP-seq data generated in a lymphoblastoid B cell line (GM12878)(46),
278 and while this data indicated promiscuous binding of all NF-κB subunits around the transcription
279 start site (TSS) of *BCL2L1* (encoding BCLXL), and no definitive binding of NF-κB subunits at the TSS
280 for *BCL2*. We did find marginally higher levels of cRel binding than both RelB and RelA at the *MCL1*
281 TSS (Figure 6A). To explore whether this bias towards NF-κB cRel was unique to the lymphoblastoid
282 cell lines we collected Model-based Analysis for ChIP-Seq 2 (MACS2) scores for NF-κB cRel, RelA
283 and RelB within 1kb of the MCL1 TSS across ChIP-Seq datasets reported in a ChIP-seq database

284 (ChIP-Atlas (47), Figure 6B). This analysis confirmed significantly higher binding of cRel to the *MCL1*
285 TSS than both RelA and RelB across multiple ChIP-seq datasets (Figure 6B, $p<0.0001$).
286 To further investigate our hypothesis, we sought an alternative method to selectively increase cRel
287 activity in B cells. Computational modelling of NF-κB in wild type (WT) B cells, IκBε knock-out B cells,
288 and B cells bearing an IκBα promoter mutation that lowered IκBα expression (IκBα$^{\kappa B/\kappa B}$), predicted that
289 IκBε$^{-/-}$ induces cRel activity significantly more than RelA activity (Figure 6D, $p<0.001$). Simulations
290 also predicted that IκBα$^{\kappa B/\kappa B}$ would increase cRel and RelA with no significant enrichment in the
291 activity of either NF-κB subunit (Figure 6D). This computational prediction was experimentally
292 validated using data from Alves *et al.* 2014 (Figure 6E) who found a similar selective induction of cRel
293 in IκBε$^{-/-}$ mouse B cells (Compare Figure 6D-6E). We therefore investigated the levels of MCL1 in
294 primary splenic B cells from WT, IκBε$^{-/-}$ and IκBα$^{\kappa B/\kappa B}$ mice (Figure 6F, 95-99% purity, supplemental
295 Figure 7), which revealed significant selective induction of Mcl1 in IκBε$^{-/-}$ cells (Figure 6G, $p<0.05$).
296 IκBα$^{\kappa B/\kappa B}$ cells showed no selectivity in the induction of BCL2-family proteins (Figure 6G). Together,
297 this ChIP-seq analysis, computational modeling, and validation in primary mouse models (Figure 6
298 D, E and G), align to implicate cRel in the upregulation of MCL1 in DLBCL.
299

300 **Inhibition of the NF-κB inducing kinase (NIK) overcomes tumor microenvironment (TME)-**
301 **mediated BH3-mimetic resistance in DLBCL**

302 Our data highlighted a key challenge, that multiple distinct and context-specific mechanisms of
303 resistance to BH3-mimetics can be identified. We sought to identify a single pharmacological
304 intervention that could overcome multiple methods of TME-mediated resistance to multiple BH3-
305 mimetics. We assessed the efficacy of NIK inhibition using Amgen16 (Figure 7A), and found the
306 inhibitor achieved significant re-sensitization of the SUDHL8 cell lines to BCLXL inhibition in hCD40L-
307 3T3 co-culture (Figure 7B, $p<0.001$). We also found that in both cell lines that were ABT199 sensitive

308 in monoculture (U2932 and RIVA), and resistant in hCD40L-3T3 co-culture, treatment with the NIK
309 inhibitor significantly reversed the ABT199 resistance (Figure 7C and D, $p<0.05$). As such, NIK
310 inhibition is effective in all cell lines tested here: either as a monotherapy in RelB high DLBCL (Figure
311 1B), to re-sensitize BCL2-sensitive DLBCL to ABT199 in the TME (Figure 7C and D), or to re-sensitize
312 BCLXL-sensitive DLBCL to BCLXL targeting BH3-mimetics in the TME (Figure 7B).
313
314 **Discussion**
315 The molecular heterogeneity that characterizes DLBCL is a major challenge contributing to clinical
316 resistance and relapse (48, 49). While there is substantial evidence that aberrant NF-κB activation
317 within the lymph node TME, confers worse prognosis in DLBCL, the pharmacological targeting of this
318 interaction has been challenging due to toxicities associated with targeting the canonical NF-κB
319 pathway (50).
320 Here we found that visualizing heterogeneity within and between DLBCL cell populations, as z-
321 scored contour plots (termed NF-κB and BCL2-family "fingerprints"), was able to identify markers of
322 drug sensitivity. We found that high RelB conferred sensitivity to inhibition of the non-canonical NF-
323 κB pathway using a NIK inhibitor. The present study indicates that flow cytometry fingerprinting may
324 enable identification and assignment of NIK-inhibitors particularly in the recently identified subset of
325 DLBCL with high RelB and poor prognosis (51).
326 BCL2 fingerprints confirmed that basal high basal BCL2 levels predicted sensitivity to ABT199, in
327 accordance with results from clinical trials (52, 53). When compared to other biochemical
328 measurements, or functional measurements such as BH3-profiling, flow cytometry-based
329 fingerprinting enables identification of cellular sub populations within a heterogeneous tumor. We
330 found that even within a single cell line we could identify multiple venetoclax resistance

331 mechanisms, with some cells inherently resistant due to high MCL1, and some cells gaining
332 resistance in the context of a TME-mimicking co-culture through upregulation of BCLXL.
333 BCL2-targeting therapies create impressive responses in CLL, where the bulk of the disease is
334 circulating in the peripheral blood, however lymph-node mediated treatment resistance has been
335 implicated in the inability to cure CLL (54). In DLBCL, where the bulk of the disease is supported by
336 the lymph node TME, BCL2-targeting therapies have been far less effective. Increased non-canonical
337 NF-κB activity, and abundance of BCLXL, may provide a rationale for the lack of efficacy of ABT199 in
338 DLBCL. The addition of the NIK inhibitor Amgen16 overcame TME-mediated protection and re-
339 sensitized DLBCL cells to ABT199. This finding is supported by studies in CLL (24, 25). Taken together
340 these data show dual potential for NIK-inhibition in DLBCL, either as a monotherapy for RelB-reliant
341 lymphoma, or as a combination therapy to overcome BH3-mimetic resistance induced by the TME.
342 We found that this effect was not restricted to BCL2-targeting therapies as NIK inhibition could re-
343 sensitize BCLXL dependent cell lines to BCLXL-inhibition in the context of TME-mimicking co-
344 culture.
345 We discovered an unexpected induction of MCL1 in cells with elevated basal NF-κB activity. This
346 result highlighted limitations in flow cytometry fingerprints in predicting cellular responses: the lack
347 of information on nuclear NF-κB activity. Incorporating NF-κB activity information into computational
348 models led to a prediction of signaling crosstalk between the two NF-κB pathways, which was
349 experimentally confirmed. It has been unclear which NF-κB subunit controls MCL1 in lymphoma
350 (55). Our combined modeling, immunofluorescence and flow cytometry data, along with published
351 ChIP-seq datasets implicate cRel as a regulator of MCL1 in DLBCL. cRel-mediated gene expression
352 has been correlated with GC-DLBCL (56), and pre-clinical MCL1 inhibitors show increased efficacy
353 in GC-DLBCL (57). As MCL1 inhibitors are currently reaching first-in-human studies (58), a predictive
354 understanding of how the TME controls abundance of anti-apoptotic proteins through NF-κB will be

355 key to successful trial design and clinical adoption. This study highlights the importance of
356 understanding the impact of TME-mediated signaling, which may not be captured in assays
357 performed on isolated cells or isolated mitochondria (59).
358 Computational simulations can: predict DLBCL responses to BH3-mimetics (35), integrate flow
359 cytometry and mutational information to predict DLBCL signaling responses to the TME (19), and
360 predict unexpected crosstalk between the TME and anti-apoptotic proteins as shown here. Higher
361 dimensional data, combining NF-κB subunit nuclear localization with BCL2-family protein
362 abundances, and integration of this data with computational modelling, enables assignment of
363 targeted therapies that can overcome the protective effect of the TME. While detailed molecular
364 characterization is unlikely to be incorporated into the standard of care for all DLBCL patients,
365 computational simulations informed by genetic profiling of diagnostic samples enable the
366 identification of DLBCL patients that are molecularly predisposed to a poor response (37). Such a
367 prediction motivates further combined molecular profiling and computational modeling in order to
368 assign efficacious targeted therapeutic approaches to the subset patients who will not respond to
369 the standard of care.

Acknowledgments

We would like to thank all members of the Mitchell and Pepper labs for valuable discussions. This study was supported by *Leukaemia UK John Goldman Fellowship 2020/JGF/003, UKRI Future Leaders Fellowship (MR/T041889/1) and Paul Stanforth PhD Studentship* (to S.M), *Blood Cancer UK 23004* (to C.P), *MRC MR/V009095/1* (to A.P), *NIH R01AI132731 and R01AI127867* (to A.H).

Data Availability Statement

The computational code and analysis pipelines generated during and/or analyzed during the current study are available in the GitHub repository, https://github.com/SiFTW/VareliEtAl/. Any other data generated during and/or analyzed during the current study are available from the corresponding author on reasonable request.

Authorship Contributions

Contribution: **A.V** designed the research, performed experiments, analyzed data, designed figures and wrote the manuscript; **H.V.N** performed experiments, cosupervised part of the study and reviewed the manuscript; **H.C, E.J, L.S** performed experiments; **H.Z., Y.L** performed experiments, analyzed data, designed figures and wrote the manuscript; **F.S** interpreted data and reviewed the manuscript; **A.H** contributed vital new reagents, interpreted data, supervised part of the study and reviewed the manuscript; **A.P, C.P** designed the research, cosupervised the study and reviewed the manuscript; **S.M** designed the research, supervised the study, performed experiments, analyzed data, designed figures and wrote the manuscript.

Disclosure of Conflicts of Interest: Yi Liu is a shareholder of DeepKinase Biotechnologies.

References

1. Davies A, Barrans S, Burton C, Mercer K, Caddy J, Chinnery F, et al. ACCEPT - combining acalabrutinib with rituximab, cyclophosphamide, doxorubicin, vincristine and prednisolone (R-CHOP) for Diffuse Large B-cell Lymphoma (DLBCL): study protocol for a Phase Ib/II open-label non-randomised clinical trial. F1000Res. 2020;9:941.
2. Meng F, Zhong D, Zhang L, Shao Y, Ma Q. Efficacy and safety of rituximab combined with chemotherapy in the treatment of diffuse large B-cell lymphoma: a meta-analysis. Int J Clin Exp Med. 2015;8(10):17515-22.
3. Feugier P, Hoof AV, Sebban C, Solal-Celigny P, Bouabdallah R, Fermé C, et al. Long-Term Results of the R-CHOP Study in the Treatment of Elderly Patients With Diffuse Large B-Cell Lymphoma: A Study by the Groupe d'Etude des Lymphomes de l'Adulte. Journal of Clinical Oncology. 2005;23(18):4117-26.
4. Tilly H, Morschhauser F, Sehn LH, Friedberg JW, Trněný M, Sharman JP, et al. Polatuzumab vedotin in previously untreated diffuse large B-cell lymphoma. New England Journal of Medicine. 2022;386(4):351-63.
5. Bartlett NL, Wilson WH, Jung S-H, Hsi ED, Maurer MJ, Pederson LD, et al. Dose-adjusted EPOCH-R compared with R-CHOP as frontline therapy for diffuse large B-cell lymphoma: clinical outcomes of the phase III intergroup trial alliance/CALGB 50303. Journal of clinical oncology. 2019;37(21):1790-9.
6. Hunter E, McCord R, Ramadass AS, Green J, Westra JW, Mundt K, et al. Comparative molecular cell-of-origin classification of diffuse large B-cell lymphoma based on liquid and tissue biopsies. Translational Medicine Communications. 2020;5(1):5.
7. Swerdlow SH, Campo E, Pileri SA, Harris NL, Stein H, Siebert R, et al. The 2016 revision of the World Health Organization classification of lymphoid neoplasms. Blood. 2016;127(20):2375-90.
8. Vaidya R, Witzig TE. Prognostic factors for diffuse large B-cell lymphoma in the R(X)CHOP era. Ann Oncol. 2014;25(11):2124-33.
9. Priebe V, Sartori G, Napoli S, Chung EYL, Cascione L, Kwee I, et al. Role of ETS1 in the Transcriptional Network of Diffuse Large B Cell Lymphoma of the Activated B Cell-Like Type. Cancers. 2020;12(7):1912.
10. Pasqualucci L, Dalla-Favera R. Genetics of diffuse large B-cell lymphoma. Blood. 2018;131(21):2307-19.
11. Chapuy B, Stewart C, Dunford AJ, Kim J, Kamburov A, Redd RA, et al. Molecular subtypes of diffuse large B cell lymphoma are associated with distinct pathogenic mechanisms and outcomes. Nature Medicine. 2018;24(5):679-90.
12. Mitchell S, Vargas J, Hoffmann A. Signaling via the NFκB system. WIREs Systems Biology and Medicine. 2016;8(3):227-41.
13. Basak S, Kim H, Kearns JD, Tergaonkar V, O'Dea E, Werner SL, et al. A fourth IκB protein within the NF-κB signaling module. Cell. 2007;128(2):369-81.
14. Alves BN, Tsui R, Almaden J, Shokhirev MN, Davis-Turak J, Fujimoto J, et al. IκBε is a key regulator of B cell expansion by providing negative feedback on cRel and RelA in a stimulus-specific manner. The Journal of Immunology. 2014;192(7):3121-32.
15. Almaden JV, Tsui R, Liu YC, Birnbaum H, Shokhirev MN, Ngo KA, et al. A pathway switch directs BAFF signaling to distinct NFκB transcription factors in maturing and proliferating B cells. Cell reports. 2014;9(6):2098-111.

16. Davis RE, Brown KD, Siebenlist U, Staudt LM. Constitutive nuclear factor κB activity is required for survival of activated B cell–like diffuse large B cell lymphoma cells. The Journal of experimental medicine. 2001;194(12):1861-74.
17. Curry CV, Ewton AA, Olsen RJ, Logan BR, Preti HA, Liu Y-C, et al. Prognostic impact of C-REL expression in diffuse large B-cell lymphoma. Journal of hematopathology. 2009;2:20-6.
18. Eluard B, Nuan-Aliman S, Faumont N, Collares D, Bordereaux D, Montagne A, et al. The alternative RelB NF-κB subunit is a novel critical player in diffuse large B-cell lymphoma. Blood, The Journal of the American Society of Hematology. 2022;139(3):384-98.
19. Jayawant E, Pack A, Clark H, Kennedy E, Ghodke A, Jones J, et al. NF-κB fingerprinting reveals heterogeneous NF-κB composition in diffuse large B-cell lymphoma. Frontiers in Oncology. 2023;13.
20. Pasqualucci L, Klein U. NF-κB mutations in germinal center B-cell lymphomas: Relation to NF-κB function in normal B cells. Biomedicines. 2022;10(10):2450.
21. Johnson PW, Balasubramanian S, Hodkinson B, Shreeve SM, Sun S, Srinivasan S, et al. Clinical impact of ibrutinib plus R-CHOP in untreated DLBCL coexpressing BCL2 and MYC in the phase 3 PHOENIX trial. Blood Advances. 2023;7(10):2008-17.
22. Younes A, Sehn LH, Johnson P, Zinzani PL, Hong X, Zhu J, et al. Randomized phase III trial of ibrutinib and rituximab plus cyclophosphamide, doxorubicin, vincristine, and prednisone in non–germinal center B-cell diffuse large B-cell lymphoma. Journal of Clinical Oncology. 2019;37(15):1285-95.
23. Studencka-Turski M, Maubach G, Feige MH, Naumann M. Constitutive activation of nuclear factor kappa B-inducing kinase counteracts apoptosis in cells with rearranged mixed lineage leukemia gene. Leukemia. 2018;32(11):2498-501.
24. Burley TA, Kennedy E, Broad G, Boyd M, Li D, Woo T, et al. Targeting the Non-Canonical NF-κB Pathway in Chronic Lymphocytic Leukemia and Multiple Myeloma. Cancers (Basel). 2022;14(6).
25. Haselager M, Thijssen R, West C, Young L, Van Kampen R, Willmore E, et al. Regulation of Bcl-XL by non-canonical NF-κB in the context of CD40-induced drug resistance in CLL. Cell Death & Differentiation. 2021;28(5):1658-68.
26. Froehlich TC, Müller-Decker K, Braun JD, Albrecht T, Schroeder A, Gülow K, et al. Combined inhibition of Bcl-2 and NFκB synergistically induces cell death in cutaneous T-cell lymphoma. Blood. 2019;134(5):445-55.
27. Bojarczuk K, Wienand K, Ryan JA, Chen L, Villalobos-Ortiz M, Mandato E, et al. Targeted inhibition of PI3Kα/δ is synergistic with BCL-2 blockade in genetically defined subtypes of DLBCL. Blood. 2019;133(1):70-80.

31. Morschhauser F, Feugier P, Flinn IW, Gasiorowski R, Greil R, Illés Á, et al. A phase 2 study of venetoclax plus R-CHOP as first-line treatment for patients with diffuse large B-cell lymphoma. Blood. 2021;137(5):600-9.
32. Davids MS, Roberts AW, Seymour JF, Pagel JM, Kahl BS, Wierda WG, et al. Phase I First-in-Human Study of Venetoclax in Patients With Relapsed or Refractory Non-Hodgkin Lymphoma. J Clin Oncol. 2017;35(8):826-33.
33. Bose P, Gandhi V, Konopleva M. Pathways and mechanisms of venetoclax resistance. Leukemia & lymphoma. 2017;58(9):2026-39.
34. Victoria MS, Anna D, Kristina H, Daniela B, Ross J, Lisa K, et al. Specific interactions of BCL-2 family proteins mediate sensitivity to BH3-mimetics in diffuse large B-cell lymphoma. Haematologica. 2020;105(8):2150-63.

35. Cloete I, Smith VM, Jackson RA, Pepper A, Pepper C, Vogler M, et al. Computational modeling of DLBCL predicts response to BH3-mimetics. NPJ Systems Biology and Applications. 2023;9(1):23.
36. Mitchell S, Tsui R, Tan ZC, Pack A, Hoffmann A. The NF-κB multidimer system model: A knowledge base to explore diverse biological contexts. Science signaling. 2023;16(776):eabo2838.
37. Norris R, Jones J, Mancini E, Chevassut T, Simoes FA, Pepper C, et al. Patient-specific computational models predict prognosis in B cell lymphoma by quantifying pro-proliferative and anti-apoptotic signatures from genetic sequencing data. Blood Cancer Journal. 2024;14(1):105.
38. Almaden JV, Tsui R, Liu YC, Birnbaum H, Shokhirev MN, Ngo KA, et al. A pathway switch directs BAFF signaling to distinct NFκB transcription factors in maturing and proliferating B cells. Cell Rep. 2014;9(6):2098-111.
39. Bian Y, Li L, Dong M, Liu X, Kaneko T, Cheng K, et al. Ultra-deep tyrosine phosphoproteomics enabled by a phosphotyrosine superbinder. Nat Chem Biol. 2016;12(11):959-66.
40. Mitchell S, Roy K, Zangle TA, Hoffmann A. Nongenetic origins of cell-to-cell variability in B lymphocyte proliferation. Proceedings of the National Academy of Sciences. 2018;115(12):E2888-E97.
41. Rackauckas C, Nie Q. Differentialequations. jl–a performant and feature-rich ecosystem for solving differential equations in julia. Journal of open research software. 2017;5(1):15-.
42. Quentmeier H, Amini RM, Berglund M, Dirks WG, Ehrentraut S, Geffers R, et al. U-2932: two clones in one cell line, a tool for the study of clonal evolution. Leukemia. 2013;27(5):1155-64.
43. Tromp JM, Tonino SH, Elias JA, Jaspers A, Luijks DM, Kater AP, et al. Dichotomy in NF-κB signaling and chemoresistance in immunoglobulin variable heavy-chain-mutated versus unmutated CLL cells upon CD40/TLR9 triggering. Oncogene. 2010;29(36):5071-82.
44. Estupiñán HY, Bouderlique T, He C, Berglöf A, Cappelleri A, Frengen N, et al. In BTK, phosphorylated Y223 in the SH3 domain mirrors catalytic activity, but does not influence biological function. Blood Adv. 2024;8(8):1981-90.
45. Homig-Holzel C, Hojer C, Rastelli J, Casola S, Strobl LJ, Müller W, et al. Constitutive CD40 signaling in B cells selectively activates the noncanonical NF-κB pathway and promotes lymphomagenesis. The Journal of experimental medicine. 2008;205(6):1317-29.
46. Zhao B, Barrera LA, Ersing I, Willox B, Schmidt SC, Greenfeld H, et al. The NF-κB genomic landscape in lymphoblastoid B cells. Cell reports. 2014;8(5):1595-606.
47. Zou Z, Ohta T, Oki S. ChIP-Atlas 3.0: a data-mining suite to explore chromosome architecture together with large-scale regulome data. Nucleic Acids Research. 2024:gkae358.
48. Coiffier B, Sarkozy C. Diffuse large B-cell lymphoma: R-CHOP failure-what to do? Hematology Am Soc Hematol Educ Program. 2016;2016(1):366-78.
49. Raut LS, Chakrabarti PP. Management of relapsed-refractory diffuse large B cell lymphoma. South Asian J Cancer. 2014;3(1):66-70.
50. Prescott JA, Cook SJ. Targeting IKKβ in Cancer: Challenges and Opportunities for the Therapeutic Utilisation of IKKβ Inhibitors. Cells. 2018;7(9):115.
51. Eluard B, Nuan-Aliman S, Faumont N, Collares D, Bordereaux D, Montagne A, et al. The alternative RelB NF-κB subunit is a novel critical player in diffuse large B-cell lymphoma. Blood. 2022;139(3):384-98.
52. Kapoor I, Bodo J, Hill BT, Hsi ED, Almasan A. Targeting BCL-2 in B-cell malignancies and overcoming therapeutic resistance. Cell Death & Disease. 2020;11(11):941.
53. Waclawiczek A, Leppä A-M, Renders S, Stumpf K, Reyneri C, Betz B, et al. Combinatorial BCL2 Family Expression in Acute Myeloid Leukemia Stem Cells Predicts Clinical Response to Azacitidine/Venetoclax. Cancer Discovery. 2023;13(6):1408-27.

531 54. Woyach JA, Johnson AJ. Targeted therapies in CLL: mechanisms of resistance and
532 strategies for management. Blood, The Journal of the American Society of Hematology.
533 2015;126(4):471-7.
534 55. Liu H, Yang J, Yuan Y, Xia Z, Chen M, Xie L, et al. Regulation of Mcl-1 by constitutive
535 activation of NF-kappaB contributes to cell viability in human esophageal squamous cell
536 carcinoma cells. BMC Cancer. 2014;14(1):98.
537 56. Faumont N, Taoui O, Collares D, Jais J-P, Leroy K, Prévaud L, et al. C-rel is the pivotal
538 NF-κB subunit in germinal center diffuse Large b-cell lymphoma: a LYSA study. Frontiers in
539 Oncology. 2021;11:638897.
540 57. Liu T, Xu F, Thieme E, Lam V, Fan G, Nikolaenko L, et al. Pharmacologic targeting MCL1
541 with AZD5991 induces apoptosis and mitochondrial dysfunction in non-Hodgkin lymphoma (NHL)
542 cells. Blood. 2020;136:33.
543 58. Desai P, Lonial S, Cashen A, Kamdar M, Flinn I, O'Brien S, et al. A Phase 1 First-in-
544 Human Study of the MCL-1 Inhibitor AZD5991 in Patients with Relapsed/Refractory Hematologic
545 Malignancies. Clinical Cancer Research. 2024:OF1-OF12.
546 59. Moore VDG, Letai A. BH3 profiling–measuring integrated function of the mitochondrial
547 apoptotic pathway to predict cell fate decisions. Cancer letters. 2013;332(2):202-5.
548

549 **Figure Legends**

550

551 **Figure 1.** NF-κB and BCL2 'fingerprinting' predicts sensitivities to inhibition of non-canonical NF-κB
552 and BCL2 in Diffuse Large B cell Lymphoma (DLBCL). (A) Representative dot plots of RelA and RelB
553 Median Fluorescence Intensity (MFI) values for the DLBCL cell lines SUDHL8, SUDHL10, U2932, and
554 RIVA. Workflow pipeline for the productions of NF-κB fingerprints. (B) Relative RelA and RelB
555 expression levels measured with flow cytometry, in the cell lines RIVA, U2932, SUDHL8 and
556 SUDHL10 as fingerprints, with dots representing the median in a single experiment, also shown as
557 probability density curves (right and top). (C) Bar graphs of RelA and RelB median fluorescence
558 intensity (MFI) values as mean ± standard deviation of two independent experiments. (*P< 0.05; one-
559 way ANOVA with Tukey's comparisons test). (D) Cell viability in response to 0.125-100μM of Amgen16
560 in the indicated DLBCL cell lines post a 24-hour treatment, error bars representing the mean ±
561 standard deviation of three independent experiments, normalized to the untreated control. (E) LC_{50}
562 values for the indicated cell lines in response to Amgen16 with mean indicated, three independent
563 experiments *(**P<0.01, ***P<0.001 unpaired T-test)*. (F) Relative MCL1, and BCL2, and BCLXL
564 expression levels measured with flow cytometry, in the cell lines RIVA, U2932, SUDHL8 and
565 SUDHL10 as fingerprints, with dots representing the median in a single experiment, also shown as
566 probability density curves (right and top). (G) Bar graphs of MCL1, and BCL2, and BCLXL median
567 fluorescence intensity (MFI) values as mean ± standard deviation of three independent experiments.
568 *(*P<0.05, **P< 0.01, ***P<0.001, ****P<0.0001; one-way ANOVA with Tukey's comparisons test*). (H)
569 Cell viability in response to 0.0001-100μM of ABT199 (venetoclax) in the indicated DLBCL cell lines,
570 post a 24-hour treatment, error bars representing the mean ± standard deviation of three
571 independent experiments, normalized to the untreated control. (I) LC_{50} values for the indicated cell
572 lines in response to ABT199 with mean indicated, of three independent experiments *(**P<0.01,*
573 ****P<0.001 unpaired T-test)*.

574 **Figure 2.** Differential BCL2 family abundance in the sub-clonal cell line U2932 predicts differential
575 responses to ABT199 (venetoclax), TME mimicking hCD40L-3T3 co-culture confers resistance to
576 BCL2 inhibition. (A) Flow cytometry dot plot showing the distinct levels of CD20 Median
577 Fluorescence Intensity (MFI) in the U2932 subclones R1 and R2. (B) Cell viability in response to
578 0.0001-100μM of ABT199in the indicated U2932 subclones R1 and R2, post 24-hour treatment, error
579 bars representing the mean ± standard deviation of three independent experiments, normalized to
580 the untreated control. (C) Bar graphs of MCL1, and BCL2, and BCLXL median fluorescence intensity
581 (MFI) values as mean ± standard deviation of three independent experiments (****P<0.0001;
582 unpaired t-test). (C) Cell viability in response to 0.0001-100μM of ABT199in the indicated U2932
583 subclones R1 and R2, post 24-hour treatment, error bars representing the mean ± standard deviation
584 of three independent experiments, normalized to the untreated control. (D) Schematic of the co-
585 culture system used. U2932 cells were co-cultured with hCD40L-3T3 cells prior to treatment with
586 increasing doses of ABT199. (E) Viability of U2932 cells cultured for 24 hours with or without CD40-
587 Ligand NIH3T3 in the presence of 0.0001-100μM of ABT199. Error bars representing the mean ±
588 standard deviation of three independent experiments, normalized to the untreated control *(**P<0.01,*
589 ****P<0.001 multiple unpaired T-tests using the Holm-Šídák corrections test)*. (F) LC50 values for the
590 U2932 cell line in monoculture vs co-culture with hCD40L-3T3 in response to ABT199, with error bars
591 representing the mean ± standard deviation of three independent experiments*(**P<0.01, unpaired T-*
592 *test). (G)* MCL1, BCL2, and BCLXL levels, shown as fold changes of 24-hour stimulation with hCD40L-
593 3T3 cells to unstimulated control in U2932 cells with error bars representing the mean ± standard
594 deviation of five independent experiments *(*P<0.1, **P<0.01 one-way ANOVA with Tukey's*
595 *comparisons test)*.
596

597 **Figure 3.** Tumor microenvironment-mimicking co-culture induced resistance to BH3-mimetics in
598 Diffuse Large B Cell Lymphoma (DLBCL) cell lines. (A) Viability of RIVA cells cultured for 24 hours with
599 or without hCD40L-3T3 cells in the presence of 0.0001-100μM of the BCL-2 inhibitor ABT199
600 (venetoclax). Error bars representing the mean ± standard deviation of three independent
601 experiments, normalized to the untreated control. (B) LC_{50} values for RIVA in each condition with error
602 bars representing the mean ± standard deviation of three independent experiments, normalized to
603 the untreated control (*$P<0.1$, unpaired T-test). (C) MCL1, BCL2, and BCLXL levels, shown as fold
604 changes of 24-hour stimulation with hCD40L-3T3 cells to unstimulated control in RIVA with error bars
605 representing the mean ± standard deviation of five independent experiments *(**$P<0.01$, ***$P<0.001$*
606 one-way ANOVA with Tukey's comparisons test. (D) Viability of SUDHL8 cells cultured for 24 hours
607 with or without hCD40L-3T3 cells in the presence of 0.0001-100μM of the BCLXL inhibitor A1331852.
608 Error bars representing the mean ± standard deviation of three independent experiments, normalized
609 to the untreated control. (E) LC_{50} values for SUDHL8 in each condition with error bars representing
610 the mean ± standard deviation of three independent experiments, normalized to the untreated
611 control (***$P<0.001$, unpaired T-test). (F) MCL1, BCL2, and BCLXL levels, shown as fold changes of
612 24-hour stimulation with hCD40L-3T3 cells to unstimulated control in SUDHL8 with error bars
613 representing the mean ± standard deviation of five independent experiments *(*$P<0.05$,* one-way
614 ANOVA with Tukey's comparisons test).
615

616 **Figure 4.** Immunofluorescence microscopy reveals differential NF-κB basal RelA activity in Diffuse
617 Large B-cell Lymphoma (DLBCL) cell lines. (A) Schematic of the canonical and non-canonical NF-κB
618 signaling pathway illustrating how non-canonical NF-κB activation results in the induction of BCLXL
619 and how elevated basal canonical signaling induces multiple negative regulators of NF-κB which may
620 contribute to cell line specific induction of MCL1. (B) Representative immunofluorescence
621 microscopy following staining in RIVA cells for RelA (NF-κB), DAPI (nucleus), actin (cytoplasm), to
622 measure nuclear and cytoplasmic subcellular localization. (C) Quantification immunofluorescence
623 microscopy showing nuclear to cytoplasmic ratio of cRel and RelA in single cells. Data shows a
624 representative replicate in the indicated cell lines. Violin width indicates data density. (D)
625 Quantification of the nuclear to cytoplasmic ratio of cRel (top) and RelA (bottom) as bar graphs with
626 error bars of the mean ± standard deviation of three independent experiments in RIVA, U2932 and
627 SUDHL8 (*P<0.1; One-Way ANOVA).
628

629 **Figure 5.** Co-culture with hCD40L-3T3 cells upregulates NF-κB RelB and BCLXL in DLBCL, and
630 selectively upregulates NF-κB cRel and MCL1 through signaling crosstalk when NF-κB RelA is
631 chronically active. (A) Abundances of the heterodimers RelA:p50 (left) and cRel:p50 (right) bound to
632 inhibiting NF-κB proteins (IκB), as simulated by computational modeling for basal canonical NF-κB
633 activation state in RIVA, and high basal activation state in SUDHL8. (B) Computational modeling
634 results showing the nuclear abundance of the indicated NF-κB dimers in a simulation with low basal
635 nuclear RelA (RIVA, pink), and a simulation high basal nuclear RelA (SUDHL8, teal). The mean (line)
636 and standard deviation (shaded region) of 25 cells is indicated. (C) Schematic demonstrating the
637 mechanism by which NF-κB contributes to the induction of BCLXL in a cell line with normal basal
638 signaling (RIVA) upon stimulation with CD40L (right). hCD40L-3T3 mediated activation of NIK results
639 in p100 processing into p52, leading to nuclear translocation of RelB:p52 and increased expression
640 of BCLXL. Gray = inactive pathways and low abundance proteins, color = active pathways and
641 predominant complexes. (D) Schematic demonstrating how crosstalk emerges between CD40, NIK,
642 cRel, and MCL1. Increase basal RelA results in increase p100, and IκBδ (left). hCD40L-3T3 mediated
643 activation of NIK results in processing of IκBδ and release of cRel:p50, which translocates to the
644 nucleus and potentially upregulates expression of MCL1 (right). Gray = inactive pathways and low
645 abundance proteins, color = active pathways and predominant complexes. (E-F) Quantification of
646 immunofluorescence microscopy in RIVA (E) and SUDHL8 (F) cells showing nuclear to cytoplasmic
647 ratio of RelA, RelB and cRel. Data post 24 hours of monoculture and hCD40L-3T3co-culture is shown
648 side by side. Single cells of a representative replicate are shown (left), with violin width indicating
649 data density. Quantification of the nuclear to cytoplasmic ratio of RelA, RelB and cRel is shown as
650 bar graphs (right) with error bars displaying the mean ± standard deviation of three independent
651 experiments (*$P<0.5$, **$P<0.01$; unpaired t-test). (G) Schematic of the co-culture system used,
652 following 24 hours of treatment with 0.0001-100μM of the BCLXL inhibitor A1331852 ± 0.1μM of the

653 Bruton's Kinase (BTK) inhibitor Ibrutinib. (H) Cell viability of SUDHL8 in response to 0.0001-100μM of
654 the BCLXL inhibitor A1331852 post a 24-hour treatment in monoculture, post a 24-hour hCD40L-
655 3T3co-culture or post a 24-hour hCD40L-3T3 co-culture with the addition of 0.1μM of the BTK
656 inhibitor, Ibrutinib. LC_{50} values for each condition is shown (right) with error bars representing the
657 mean ± standard deviation of three independent experiments, normalized to the untreated control
658 (****P<0.001* one-way ANOVA with Tukey's comparisons test).
659

660 **Figure 6.** IκBε knock-out mouse model reveals cRel-dependent induction of MCL1. (A) NF-κB ChIP-
661 seq data from Zhao et al. 2014 (47) showing binding of the indicated NF-κB subunits around the
662 transcription start site (TSS) of the indicated anti-apoptotic genes in lymphoblastoid B cell line. A 1kb
663 window around the TSS is indicated. (B) Model-based Analysis for ChIP-Seq 2 (MACS2) scores for the
664 indicated NF-κB subunits within 1kb of the MCL1 promoter across all ChIP-Seq datasets reported in
665 ChIP Atlas Zou et al. 2024 (47), after outlier removal using ROUT method (q=1%, ****p<0.0001). (C)
666 Schematic of normal basal NF-κB signaling (left), schematic of NF-κB signaling predicting the
667 unknown effect of IκBε$^{-/-}$ on cRel and MCL-1 induction. (D) Computational modelling simulation of
668 RelA and cRel abundance in IκBε$^{-/-}$ and IκBα$^{κB/κB}$ demonstrated as fold changes normalized to wild-
669 type. Error bars represent the mean and ± standard deviation of 25 cells *(****P<0.001*, unpaired t-test).
670 (E) RelA and cRel abundances in IκBε$^{-/-}$ and IκBα$^{κB/κB}$ cells derived from primary splenocytes,
671 demonstrated as fold changes to wild-type, error bars representing the mean ± standard deviation.
672 (F) Experimental pipeline showing the workflow of isolating and purifying primary B cells from wild
673 type, IκBε$^{-/-}$ and IκBα$^{κB/κB}$ mouse genotypes. (G) Abundances of MCL1 and BCLXL acquired with flow
674 cytometry in primary B cells isolated and purified from IκBε$^{-/-}$ (left) and IκBα$^{κB/κB}$ (right) mouse
675 genotypes, demonstrated as fold changes normalized to wild-type. Error bars represent the mean ±
676 standard deviation of three independent experiments (**P<0.05*, unpaired t-test).
677

678 **Figure 7.** Targeting the NF-κB inducing kinase (NIK) to overcome tumor microenvironment (TME)
679 resistance in Diffuse large B cell lymphoma (DLBCL). (A) Schematic of the co-culture system used,
680 following 24 hours of treatment with 0.0001-100μM of venetoclax (ABT199) or A1331852 ± 50μM of
681 the NIK inhibitor Amgen16 . (B) Cell viability of SUDHL8 in response to 0.0001-100μM of A1331852
682 post a 24-hour treatment in monoculture, post 24-hour co-culture on hCD40L-3T3 cells or post 24-
683 hour hCD40L-3T3 co-culture with the addition of 50μM of the NIK inhibitor Amgen16. LC_{50} values for
684 each condition is shown (right) with error bars representing the mean ± standard deviation of three
685 independent experiments, normalized to the untreated control (****P<0.001* one-way ANOVA with
686 Tukey's comparisons test). (C) U2932 and (D) RIVA cells in response to 0.0001-100μM of ABT199 in
687 the cell lines post a 24-hour treatment in monoculture, post a 24-hour hCD40L-3T3 co-culture or
688 post 24-hour hCD40L-3T3 co-culture with the addition of 50μM of the NIK inhibitor, Amgen16. LC_{50}
689 values for each condition is shown (right) with error bars representing the mean ± standard deviation
690 of three independent experiments, normalized to the untreated control (**P<0.1, **P<0.01* one-way
691 ANOVA with Tukey's comparisons test).

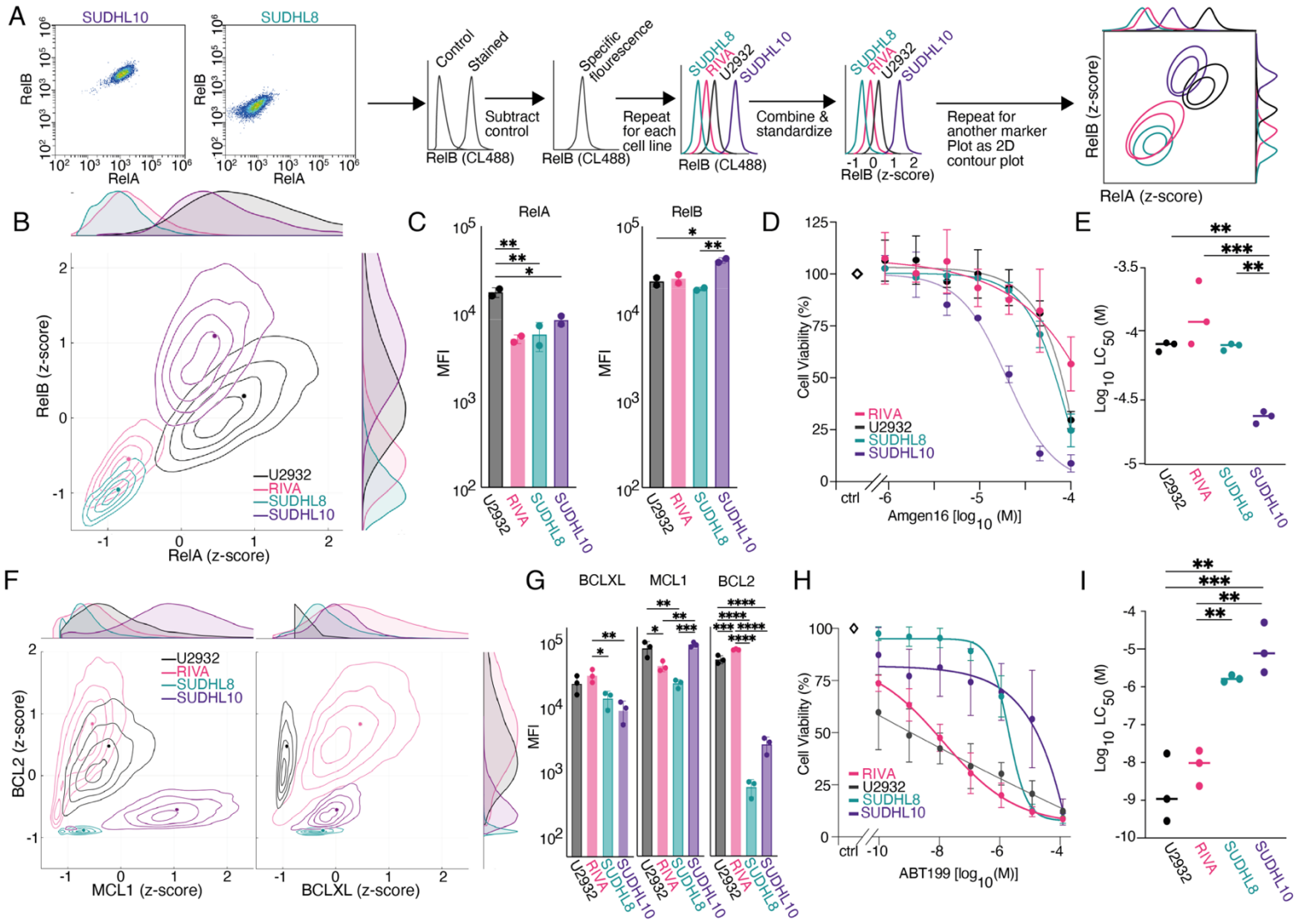
A
SUDHL10
SUDHL8
RelB
RelA
Control
Stained
Subtract control
RelB (CL488)
Specific flourescence
Repeat for each cell line
SUDHL8
RIVA
U2932
SUDHL10
Combine & standardize
RelB (z-score)
Repeat for another marker Plot as 2D contour plot
RelA (z-score)
B
RelB (z-score)
RelA (z-score)
U2932
RIVA
SUDHL8
SUDHL10
C
RelA
RelB
MFI
D
Cell Viability (%)
Amgen16 [log10 (M)]
ctrl
E
Log10 LC50 (M)
F
BCL2 (z-score)
MCL1 (z-score)
BCLXL (z-score)
G
BCLXL
MCL1
BCL2
H
ABT199 [log10(M)]
I

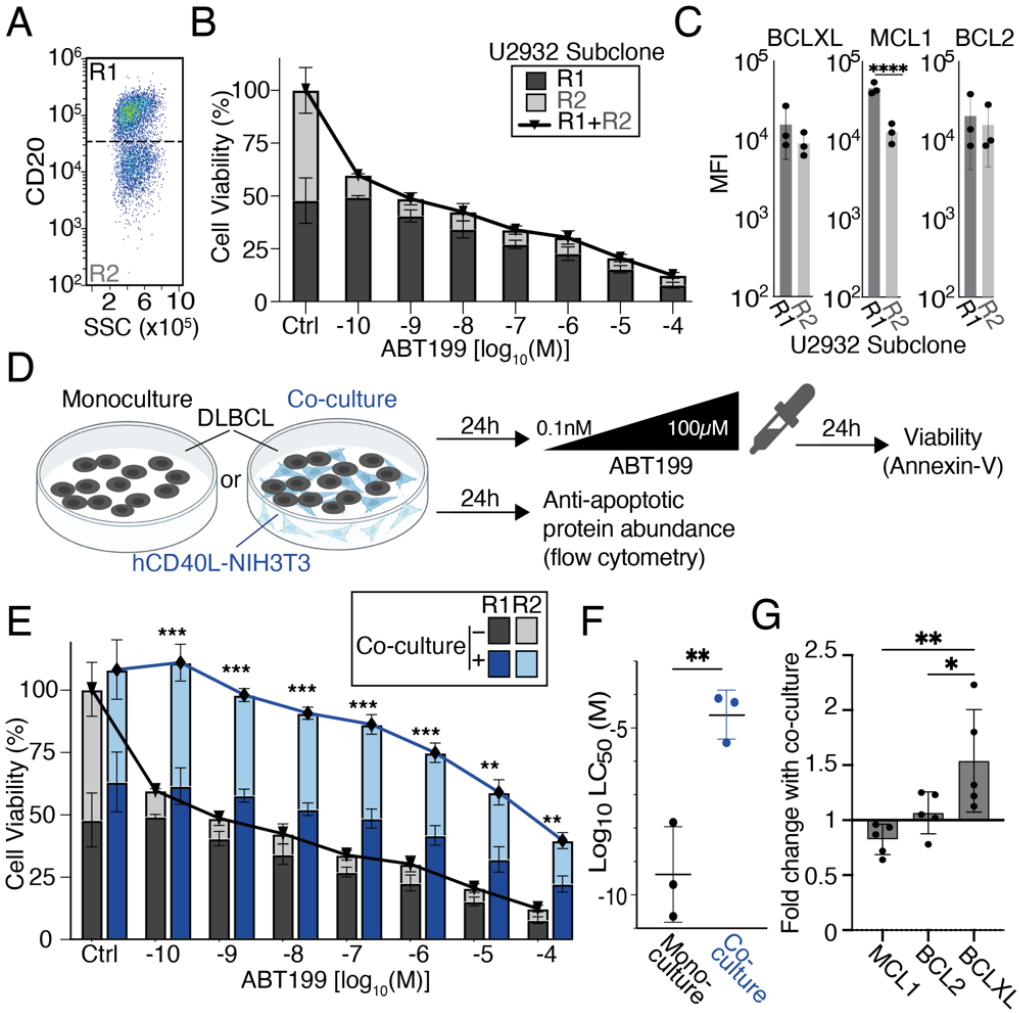
A
B
C
D
E
F
G
R1
R2
CD20
SSC (x10⁵)
Cell Viability (%)
U2932 Subclone
R1
R2
R1+R2
Ctrl
-10
-9
-8
-7
-6
-5
-4
ABT199 [log10(M)]
BCLXL
MCL1
BCL2
MFI
U2932 Subclone
Monoculture
DLBCL
Co-culture
or
hCD40L-NIH3T3
24h
0.1nM
100μM
ABT199
Viability
(Annexin-V)
Anti-apoptotic
protein abundance
(flow cytometry)
Co-culture
Log10 LC50 (M)
Mono-culture
Co-culture
Fold change with co-culture
MCL1
BCL2
BCLXL

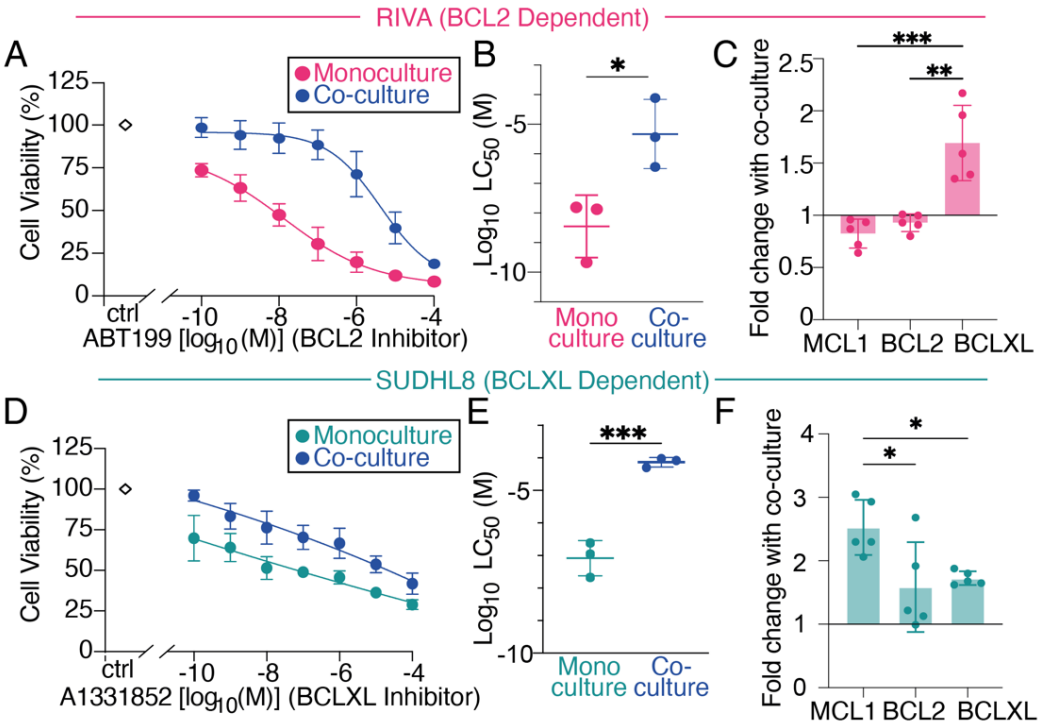
RIVA (BCL2 Dependent)
A
Monoculture
Co-culture
Cell Viability (%)
125
100
75
50
25
0
ctrl
-10
-8
-6
-4
ABT199 [log10(M)] (BCL2 Inhibitor)
B
*
Log10 LC50 (M)
-5
-10
Mono culture
Co-culture
C
***
**
Fold change with co-culture
2.5
2
1.5
1
0.5
0
MCL1
BCL2
BCLXL
SUDHL8 (BCLXL Dependent)
D
Monoculture
Co-culture
Cell Viability (%)
125
100
75
50
25
0
ctrl
-10
-8
-6
-4
A1331852 [log10(M)] (BCLXL Inhibitor)
E
***
Log10 LC50 (M)
-5
-10
Mono culture
Co-culture
F
*
*
Fold change with co-culture
4
3
2
1
0
MCL1
BCL2
BCLXL

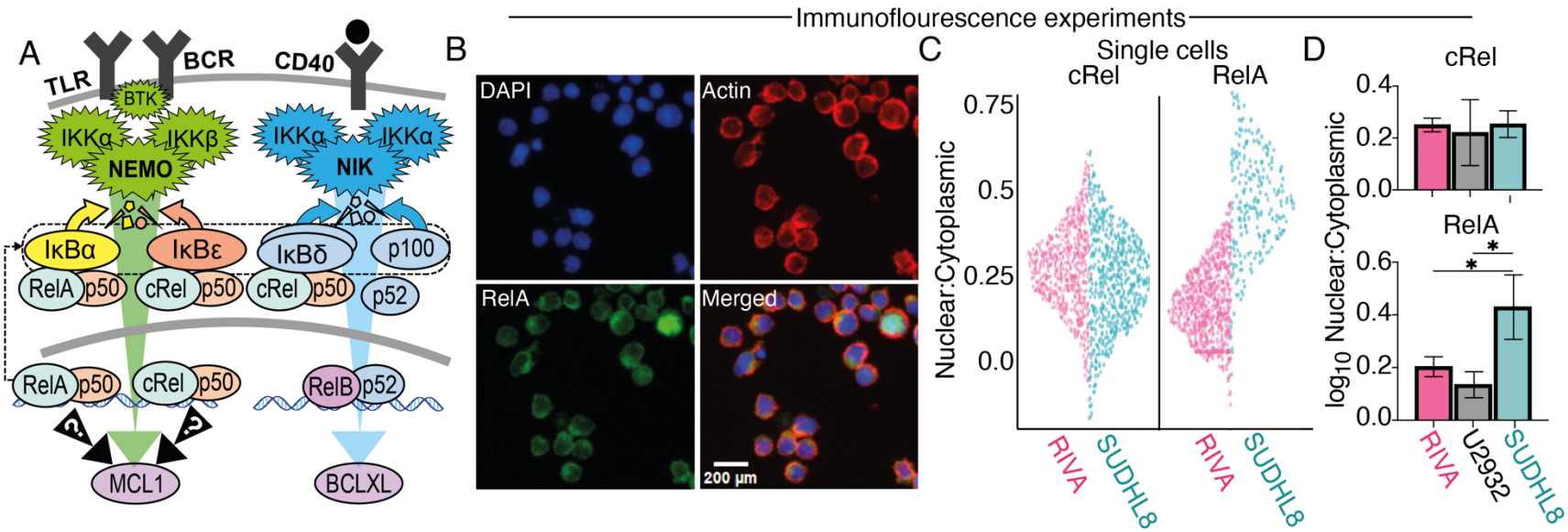
A
TLR
BCR
CD40
BTK
IKKα
IKKβ
NEMO
IKKα
IKKα
NIK
IκBα
IκBε
IκBδ
p100
RelA
p50
cRel
p50
cRel
p50
p52
RelA
p50
cRel
p50
RelB
p52
?
?
MCL1
BCLXL
B
Immunoflourescence experiments
DAPI
Actin
RelA
Merged
200 µm
C
Single cells
cRel
RelA
Nuclear:Cytoplasmic
0.75
0.5
0.25
0.0
RIVA
SUDHL8
RIVA
SUDHL8
D
cRel
RelA
log10 Nuclear:Cytoplasmic
0.4
0.2
0.0
0.6
0.4
0.2
0.0
*
*
RIVA
U2932
SUDHL8

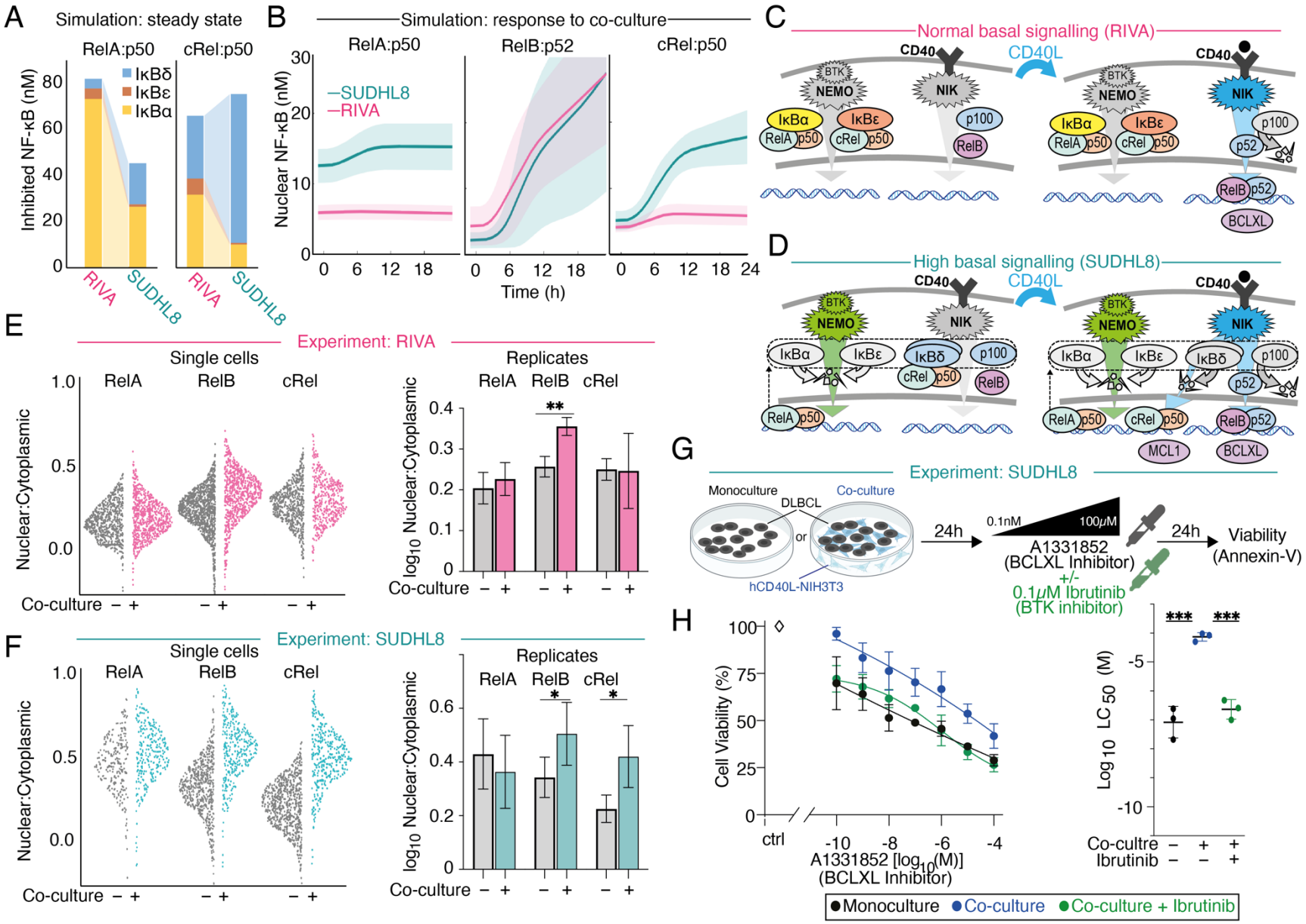
A
Simulation: steady state
RelA:p50
cRel:p50
IκBδ
IκBε
IκBα
Inhibited NF-κB (nM)
RIVA
SUDHL8
B
Simulation: response to co-culture
RelA:p50
RelB:p52
cRel:p50
SUDHL8
RIVA
Nuclear NF-κB (nM)
Time (h)
C
Normal basal signalling (RIVA)
CD40
CD40L
BTK
NEMO
NIK
IκBα
IκBε
RelA
p50
cRel
p100
RelB
p52
BCLXL
D
High basal signalling (SUDHL8)
IκBδ
MCL1
E
Experiment: RIVA
Single cells
Replicates
RelA
RelB
cRel
Nuclear:Cytoplasmic
log10 Nuclear:Cytoplasmic
Co-culture
F
Experiment: SUDHL8
G
Monoculture
Co-culture
DLBCL
or
hCD40L-NIH3T3
24h
0.1nM
100μM
A1331852
(BCLXL Inhibitor)
+/-
0.1μM Ibrutinib
(BTK inhibitor)
Viability
(Annexin-V)
H
Cell Viability (%)
ctrl
A1331852 [log10(M)]
(BCLXL Inhibitor)
Log10 LC50 (M)
Co-cultre
Ibrutinib
Monoculture
Co-culture
Co-culture + Ibrutinib

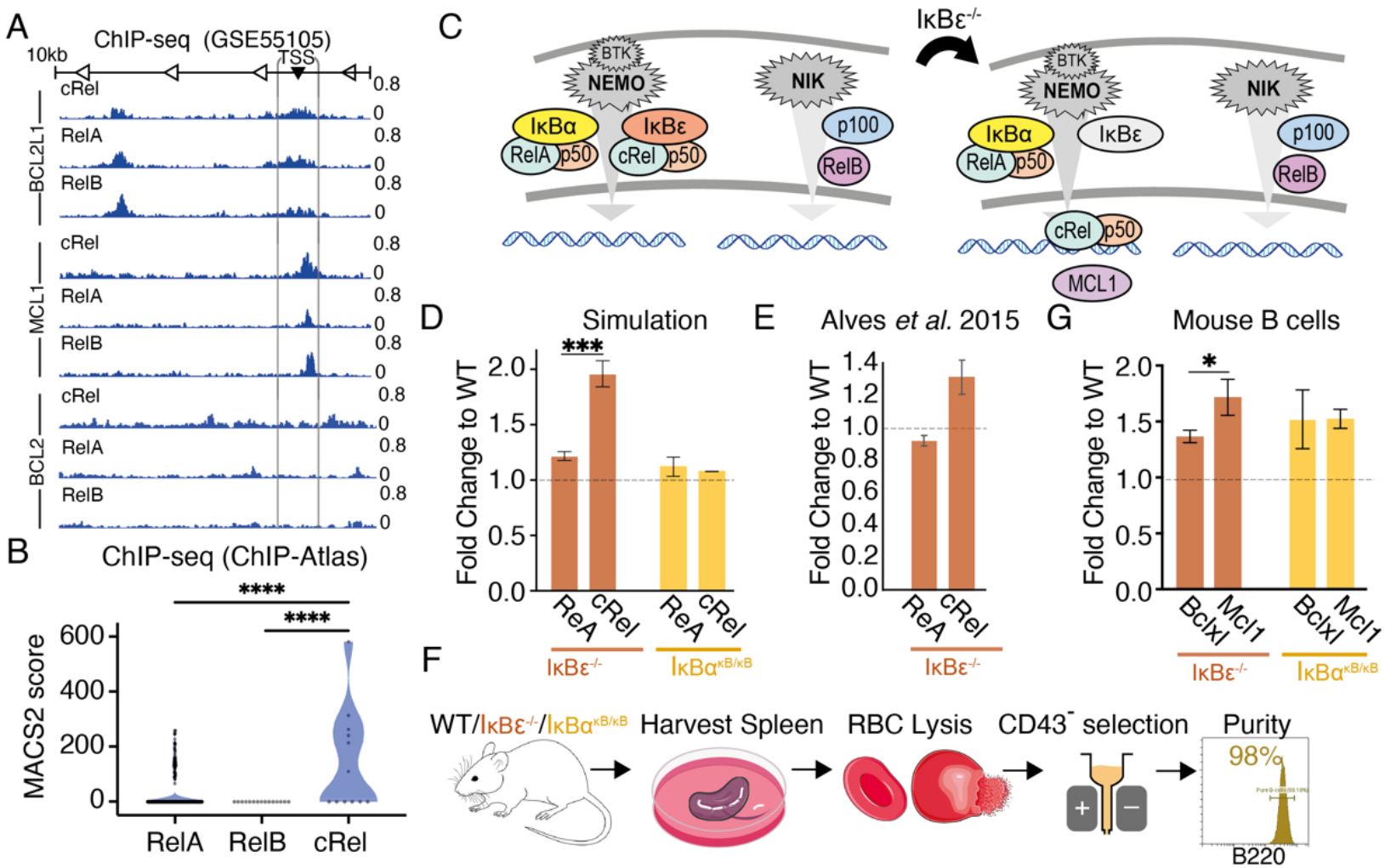
A
ChIP-seq (GSE55105)
10kb
TSS
cRel
RelA
RelB
BCL2L1
MCL1
BCL2
B
ChIP-seq (ChIP-Atlas)
MACS2 score
RelA
RelB
cRel
C
IκBε-/-
BTK
NEMO
NIK
IκBα
IκBε
RelA
p50
cRel
p100
RelB
MCL1
D
Simulation
Fold Change to WT
ReA
cRel
IκBε-/-
IκBα κB/κB
E
Alves et al. 2015
G
Mouse B cells
Bclxl
Mcl1
F
WT/IκBε-/-/IκBα κB/κB
Harvest Spleen
RBC Lysis
CD43- selection
Purity
98%
B220

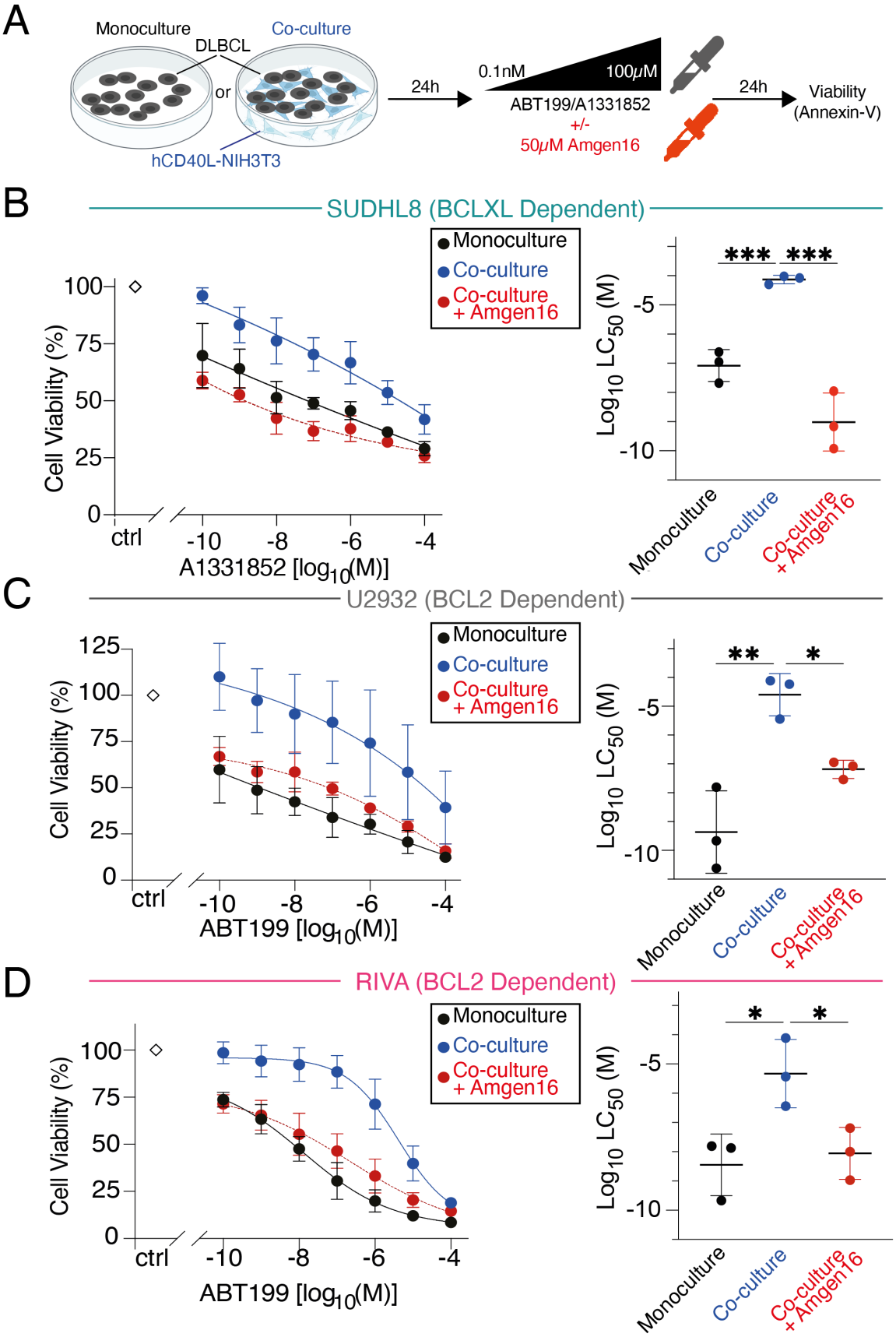
A
Monoculture
Co-culture
DLBCL
or
hCD40L-NIH3T3
24h
0.1nM
100μM
ABT199/A1331852
+/-
50μM Amgen16
24h
Viability
(Annexin-V)
B
SUDHL8 (BCLXL Dependent)
Monoculture
Co-culture
Co-culture + Amgen16
Cell Viability (%)
ctrl
A1331852 [log10(M)]
Log10 LC50 (M)
***
***
C
U2932 (BCL2 Dependent)
ABT199 [log10(M)]
**
*
D
RIVA (BCL2 Dependent)
ABT199 [log10(M)]
*
*